NDT&E International 86 (2017) 140–152

Contents lists available at ScienceDirect

NDT&E International

journal homepage: www.elsevier.com/locate/ndteint

Non-destructive thermal-wave-radar imaging of manufactured green powder metallurgy compact flaws (cracks)

A. Melnikov[a], K. Sivagurunathan[a], X. Guo[a], J. Tolev[a], A. Mandelis[a,*], K. Ly[b], R. Lawcock[b]

[a] Center for Advanced Diffusion-Wave and Photoacoustic Technologies (CADIPT), University of Toronto, 5 King's College Road, Toronto, ON M5S 3G8, Canada

[b] Stackpole International, 2430 Royal Windsor Drive, Mississauga, ON L5J 1K7, Canada

ARTICLE INFO

Keywords:
Cracks
Non-contact
Thermal wave radar imaging
Automatic defect recognition
Automotive manufacturing

ABSTRACT

Thermal wave radar imaging (TWRI) was developed to detect manufacturing cracks in automotive powder metallurgy components (transmission sprockets) in their green (unsintered) state. The crack detection capability of the TWRI phase was validated by two sets of cracked/crack-free green and sintered sprockets which were sectioned after TWRI measurements. An automatic defect recognition (ADR) TWR image processing method was also developed to differentiate cracks from local defects. Measurement results demonstrated that TWRI is superior to conventional lock-in thermography imaging (LITI) in both flaw detection resolution and speed, and thus is a viable green-sprocket manufacturing flaw imaging technology.

1. Introduction

Automotive industry utilization of powder metallurgy (PM) technology is increasing in popularity due to requirements for intricate and dimensionally accurate neat-shaped components which can be produced at competitive cost. The manufactured components, such as sprockets (for automatic transmissions and transfer cases), clutch plates (for automatic transmissions) clutch hubs (for transfer cases), synchronizer hubs (for manual transmissions) and other parts usually operate under high loads. Failure of any of the above mentioned components may cause transmission or transfer-case failure, hence loss of functionality for the vehicle. Therefore, quality and integrity requirements are high. A most important defect type in these manufactured parts is the possibility of incipient (surface breaking or subsurface) cracks present in high-stress areas such as at angles and steps [1]. PM components are formed by multi-ton pressing on the metal powder-lubricant compound. Crack appearance in a green part is related both to the powder materials and problems with the adjustment of the press equipment. Once created during the forming process, the cracks remain (often unchanged in size) after sintering. These cracks can cause component fracture in-application, possibly resulting in loss of vehicle driving power.

The PM automotive parts manufacturing industry uses various non-destructive testing (NDT) methods (acoustic, magnetic, fluorescent liquid penetrants, microscopy) to diagnose defective elements not in the "green" state but only after sintering. Nowadays, with the dramatic increase in global energy prices, international economic upheavals, and the recent serious downturn in the North American automotive industry, it is ill-afforded and expensive for the industry to dispose of, and effectively waste, defective sintered components. A highly desirable alternative solution to this problem would be the detection of the presence of cracks in automotive parts in the green state. Then, the identified defective parts can be easily reduced to metal powder which can be recycled by the manufacturer and produce new components. However, to the best of our knowledge, until now there exist no effective NDT techniques which can detect cracks in the un-sintered manufactured state. Infrared imaging has often been used as a NDT technique to detect cracks. Two crack detection mechanisms behind the technique have been identified by Bodnar et al. [2,3] and further investigated by Burrows et al. [4]: (1) rise in temperature near the crack edges due to crack-blocked lateral heat flow when the laser spot is incident on the side of crack; (2) crack-induced strong laser absorption and therefore high temperature rise when the laser spot is on the crack. In both situations the net result is enhanced thermal infrared photon (Planck) emission compared to non-cracked regions which defines the image contrast. In recent years, the technique of infrared thermographic imaging has been applied to manufactured automotive parts inspection. A dynamic frequency-domain form of this imaging method, lock-in thermography (LIT), has been developed [5–8], and used by Böhm et al. [9] to inspect adhesively bonded parts. Netzelmann used flying-spot (moving laser beam) lock-in thermography to detect cracks in steel [10]. Those researchers estimated the attainable depth of flaw

* Corresponding author.
E-mail address: mandelis@mie.utoronto.ca (A. Mandelis).

http://dx.doi.org/10.1016/j.ndteint.2016.12.004
Received 27 July 2016; Received in revised form 7 December 2016; Accepted 14 December 2016
Available online 20 December 2016
0963-8695/

detection to be ca. 3 mm in plastics, 6 mm in fiber reinforced plastics and 12 mm in metals. However, this range of depths does not easily apply to hairline (~20–100 μm wide) cracks and powder metallic compacts because of the diffusive nature of thermal waves (poor spatial and axial resolution) and the relatively poor thermal properties and rough surfaces of these materials. Early on it was recognized that LIT (more generally: photothermal) phase imaging is superior to amplitude imaging for NDT applications [11] as it yields pure thermal-wave images based only on thermophysical property contrast and higher depth resolution; it is less affected by non-uniform heating, surface emissivity variations and optical reflectivity [12,13]. Other thermal and thermally-mediated non-destructive imaging (NDI) methodologies have been developed (pulsed thermography (PT), step thermography (ST) and vibrothermography (VT), to name the most popular) [14].

The first - and, to our best knowledge, the only- attempts to apply infrared thermography to green PM compacts have been reported by Benzerrouk and Ludwig [15]. These authors made an extensive comparative study of most available NDT methods which could potentially be used for green PM compact inspection (Eddy current, ultrasound, acoustic resonance, x-rays, resistivity and thermography) [16,17]. They came to the conclusion that infrared imaging was the only method capable of testing green state compacts under realistic industrial conditions and under the desired inspection speed conditions. Their thermographic method consists of electrically resistive (Joule) heating of a green part and detection of the temperature rise by means of a mid-infrared camera which captures Planck emissions from the heated surface. The electro-thermally generated steady-state temperature field is calculated analytically or through a finite-element formulation and defects (cracks) are identified through the perturbation they cause to the (known or theoretically expected) temperature field of intact samples. The method can also be extended to dynamic electro-thermography through the use of pulsed electric fields [15]. The major problems with this arrangement are a) the cumbersome requirement for contacting electric power-generating caps to which the geometry of the inspected parts must conform: It appears that cylindrical sample geometries are best for this method; b) the very low subsurface defect contrast due to the diffusive dc thermal field which limits the detection depth range to < 20 μm, essentially confining the technique to ultrashallow surface-breaking crack detection; c) imposition of electrical conductivity value-range requirements so as to induce adequate electrical heating for thermographic imaging; and d) the lack of depth profilometry, a feature that can be attained only with frequency-scanned thermal waves or with dynamic transient thermography, provided there is effective time slicing leading to adequate axial resolution, a non-trivial condition in diffusive fields.

To substantially improve the disadvantages of LIT, our group has developed a novel imaging extension of the photothermal radiometry (PTR) method: the thermal-wave radar (TWR). In this paper we report the detection of the presence of subsurface cracks in green automotive parts with a camera-based Thermal-Wave Radar Imager (TWRI) and the specifications for fast in-line inspection.

2. The principle of TWRI flaw (crack) detection

Thermal wave imaging is an infrared non-destructive extension of PTR. Its crack detection ability in manufactured solids is based on probing subsurface and surface-breaking cracks at high-stress regions of automotive parts using laser-induced thermal waves in the vicinity of the crack (within one thermal diffusion length, μ, see definition below) by means of harmonic heat source modulation which generates periodic heat conduction ("thermal wave"), reaching the subsurface crack location by varying the modulation frequency of the source (usually a laser beam). The presence of a crack amounts to a thermal boundary impedance and is sensed through confinement (accumulation) of the thermal wave at the crack. Sensitivity is highest when the thermal wavelength is on the order of the crack size (width). Interaction with the flaw changes the amplitude and phase of the detected signal. The detected thermal wave is "depth integrated", a depth integral extending from the surface down to approx. one thermal diffusion length, μ, defined by the laser intensity modulation frequency f: $\mu(f) = (\alpha/\pi f)^{1/2}$, where α is the thermal diffusivity [cm^2/s] of the medium. Signal changes carry information about the subsurface crack region which affects thermal-wave propagation, and depend on differences between the thermal parameters (diffusivity, effusivity) of the surrounding material and those of the crack, as well as on the position, orientation and geometry of the crack [18]. Major factors limiting detectivity of near-subsurface narrow manufacturing-induced cracks (a few microns wide) using harmonic thermal waves are: a) the depth-integrated and depthwise exponentially damped nature of the signals [19,20]; b) their highly dispersive nature which results in very poor axial resolution; c) the low signal-to-noise ratio (SNR); d) the unknown depth of cracks which can be easily missed with single frequency dynamic thermography that fixes the probe depth approximately to the value of the thermal diffusion length and may miss deep flaws located directly below the laser probe; and e) the long duration of PTR frequency scans (15 – 20 min). To overcome these adverse factors, the concept of the linear frequency modulated (LFM) continuous-wave (CW) radar was combined with frequency domain photothermal physics, thereby introducing *the thermal-wave radar (TWR),*Fig. 1 [21]. The presence of subsurface discontinuities can be enhanced considerably through signal generation and processing techniques similar to the ultrasonic radar [22]. In this mode, a linear frequency sweep *("chirp")* modulates the source (e.g. laser intensity) and a cross-correlation (CC) processing algorithm with a *"matched filter"* generates CC signal peaks, Fig. 1 (bottom trace)**,** resulting in high axial resolution and depth range superior to LIT inside a sample. Higher frequencies correspond to earlier signal capture times (and shallower depths), and vice versa through a Fourier transformation. The earliest reports on LFM of thermal waves and use of radar signal (cross-correlation) processing methods appeared in a series of 1986 articles by our group using photothermal beam deflection [23–25]. Subsequently, Mulaveesala *et al.*[26] presented a similar approach using infrared thermography. The algorithm shown in Fig. 1(a) can be used to obtain depth-resolved photothermal information instead of the conventional depth-integrated LIT response by progressively delaying the matched filter and registering signals coherent to it. This can be done through CC, extensively used for signal detection in CW radars, between a judiciously delayed replica of the incident wave controlled by the operator and the generated signal [27–29]. The CC can be tuned to a particular signal arrival delay time, τ_p, corresponding to a fixed depth below the interrogated surface, while efficiently zeroing or greatly minimizing contributions from arrivals at earlier and later times which tend to dominate and mask contributions from the given depth due to the axial superposition of signal-generating sources in depth-integrating LIT. In Fig. 1 the schematic CC signal peak delay time and phase plots show the responses of thermal-wave accumulation/depletion due to discontinuities near (solid line) and farther below (dashed line) the interrogated surface. *Pulse compression* can make the width of the peak narrower (better axial resolution) and its height larger (better SNR). To meet fast industrial inline inspection requirements, a camera-based TWRI is developed for manufactured component crack detection in green sprockets.

3. Materials and methods

3.1. Powder metallurgy samples

The samples under investigation are typical products of the automotive industry, that is, sprockets with a circular geometry, Fig. 2(a), and five main regions (hub, web, spline, flange and counterbore), Fig. 2(b). Flaws (cracks) usually appear at the high-stress intersections of two perpendicular regions, or corners (web-counterbore, web-spline

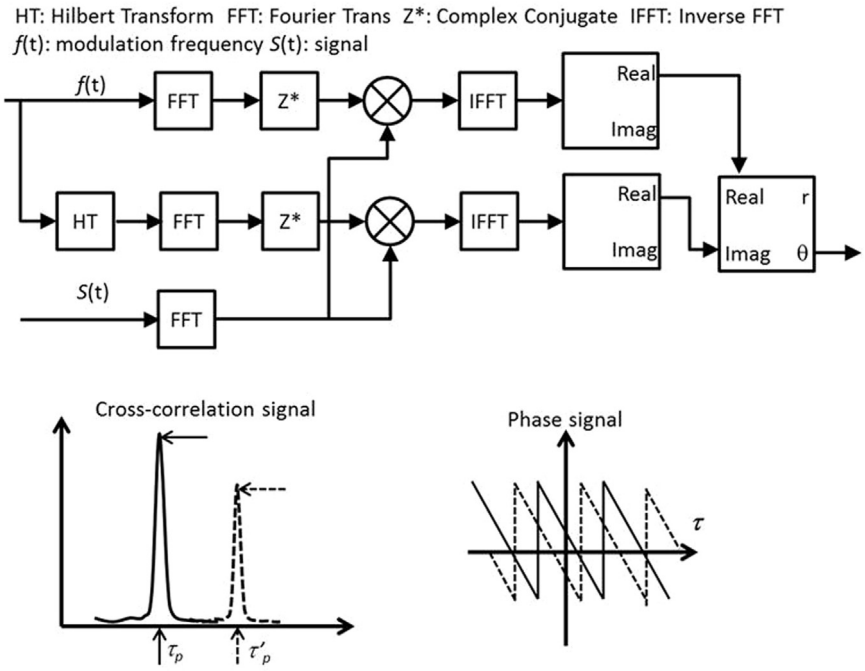

Fig. 1. TWR principle: algorithm, schematic CC signal peak delay time and phase plot.

and web-hub) as marked in Fig. 2(b). Three sets of samples were inspected: Sc1/Snc1, Sc2/Snc2, and Sc3/Snc3. Sc samples were identified by their manufacturer as cracked (with distinguishable open cracks) in the web-counterbore region and Snc samples as non-cracked (crack-free) sprockets, otherwise identical to Sc. All sets of samples were inspected with TWRI in their green state at the same web-counterbore locations. For validation purposes, samples in the first set (Sc1/Snc1) were subsequently sintered, re-inspected with TWRI, and cross-sectioned. Optical microscopic photographs of the cross sections were also taken. Samples in the second set (Sc2/Snc2) were sectioned in their green state after TWRI measurements and optical microscope photographs of the cross sections were taken.. For comparison, the first sets of samples were inspected with both TWRI and LITI. Sample sets Sc3/Snc3 were only inspected with TWRI without further sectioning.

3.2. TWRI/LITI system setup

In order to compare TWRI measurement results with conventional lock-in thermographs, a combined TWRI/LITI system was built, Fig. 3: A modulated laser beam illuminated and heated the PM sample, and the IR emission from the sample was captured by the IR camera. The main components of the TWRI/LITI system (Fig. 3(a) and their properties are listed below:

(1). Laser: 808 nm solid state laser (JOLD-45-CPXF-1 L, Jenoptik, Germany), with 45 W mapower. The laser beam size after the diffuser had ~3.4 cm dia. Laser power density on the sample was ~0.68 W/cm^2. The sample temperature during inspection was measured to be ~40 °C which was low enough so that no change of the green sample properties was measured. Laser modulation frequency ranged between 0.3 and 15 Hz. (2). IR camera (Titanium 520 M, Cedip Infrared Systems, France): 3.6–5.1 μm spectral range, 360 frame rate with lock-in connection, image size was 6.25 mm×5.4 mm with a 160×128 pixel window. (3). Motorized multi-axis sample holder: Because of the complex geometry of the regions of interest (ROI), a 6-axis (x-y-z, pitch α, roll β and yaw γ) sample holder with angular scanning automation was designed, Fig. 3(b), to meet the need for fast and flexible sample imaging, Fig. 3(c). Additionally, two visible-range cameras were installed, one camera on one side of the set-up to view and monitor the inspected site, and the other camera on top of the mid-IR camera for autofocusing. Motor axes "X" and "Z" could be used to position the sample stage to face the IR camera; motor axis "Y" could move the sample stage towards the IR camera. The horizontal rota-

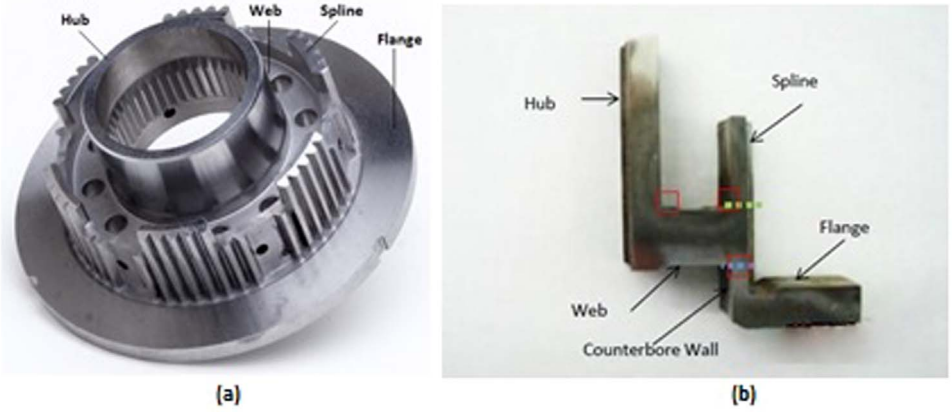

Fig. 2. (a) geometry of a sprocket, a typical sample for TWRI inspection; (b) cross section of the sample with the high-stress regions of interest marked with squares.

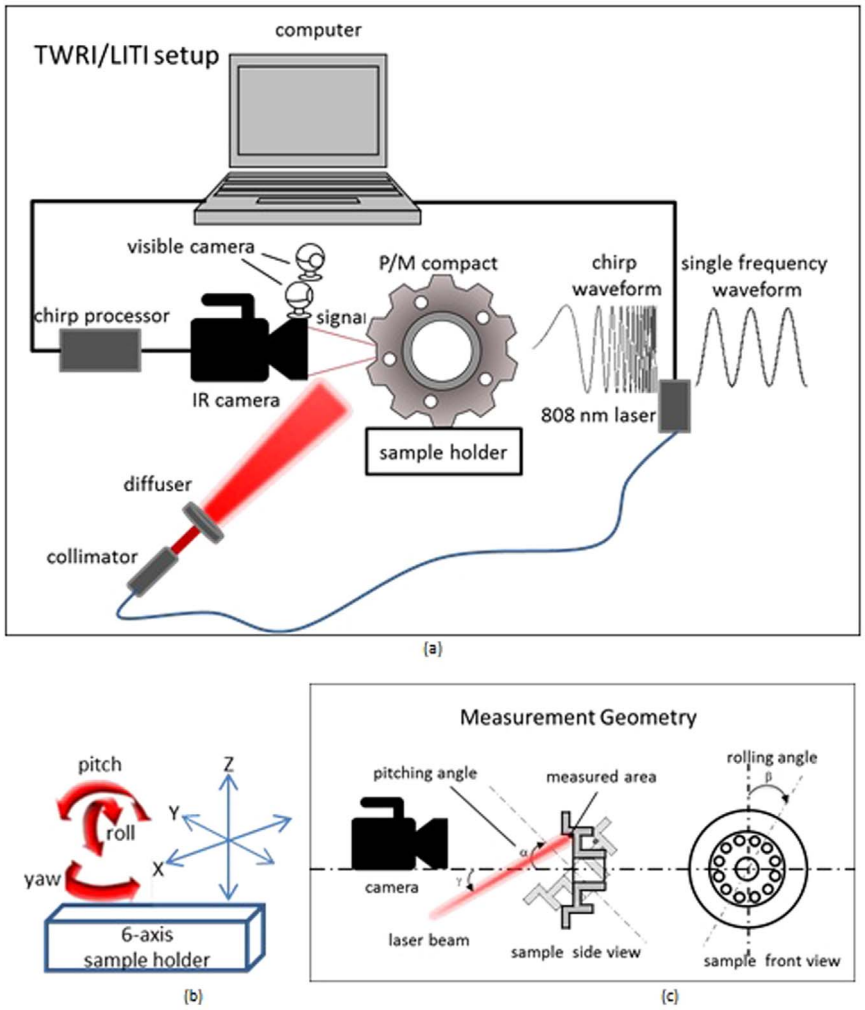

Fig. 3. TWRI/LITI system. (a) TWRI/LITI system; (b) 6-axis sample holder; (c) flexible measurement geometry diagram.

tional axis (yaw) mounted on the "Y" axis could be used to direct laser light on a ROI in the test sample. It could also be used to rotate the sample 15 degrees to face the monitoring visible-range camera on the side, so that a sample photograph with high image resolution could be captured and saved as a reference picture for each IR image. The vertical rotational axis (roll) mounted on the "Z" axis could also be used for continuous circular image scanning. The tilt axis (pitch) was used to obtain better IR images from geometrically challenging (e.g. deeply recessed) corner ROI as shown in Fig. 3(c). An additional set of x-y-z axes and a pitch axis were also installed on the IR camera and tested as an alternative for future in-line inspection. They are not shown in Fig. 3. (4) chirp/single-sine wave generator: A National Instrument card NI USB-6229 was used. (5) laser beam diffuser: A circular pattern engineered diffuser (ED1-C20, Thorlabs, NJ, USA) was installed to eliminate image artifacts resulting from uneven heating by the laser beam. (6) The experimental system inspection control and image data processing functions were performed by a computer station system through a data acquisition/generation device NI USB-6229 BNC, National Instrument Inc. with in-house developed LIT and TWR software designed for LabView environment specifically for this application.

4. Results and discussion

4.1. Flaw contrast optimization

For maximum contrast, the imaging conditions (parameters), such as laser illumination, observation angle, and modulation frequency range, were investigated and the optimal values were obtained.

4.1.1. Laser source location and illumination uniformity

To improve TWR/LIT image contrast, two laser illumination methods were explored: directly on, or off, the open crack region. On-crack illumination used the laser beam diffuser to homogenize the beam which illuminated the entire ROI (~ 6.25 mm×5 mm) and generated backscattered infrared radiation from every point as illustrated in Fig. 3(a) and (b). Off-crack illumination used partly focused laser radiation located close to the investigated area of the sample. It generated laterally propagating thermal waves that interacted sideways with the crack, including its subsurface boundaries. It was found that off-crack illumination generates better contrast than on-crack illumination, but it is hard to apply in practice because the location of the crack is unknown. So the on-crack illumination was used in all subsequent measurements.

4.1.2. Sample orientation and modulation frequency bandwidth

To maximize the probability of detecting cracks, cross-sectional camera pixel profiles of TWR/LIT images across the web-counterbore inner corner were found to be extremely useful in optimizing the observation angle and modulation frequency band as shown in Figs. 4 and 5, where each curve is the average value of 6-adjacent column pixels, displayed along a distance covering 2.5 mm along each vertical wall and across the 90° corner. Crack presence and position (indicated by sharp amplitude and phase peaks) are identified by comparing the

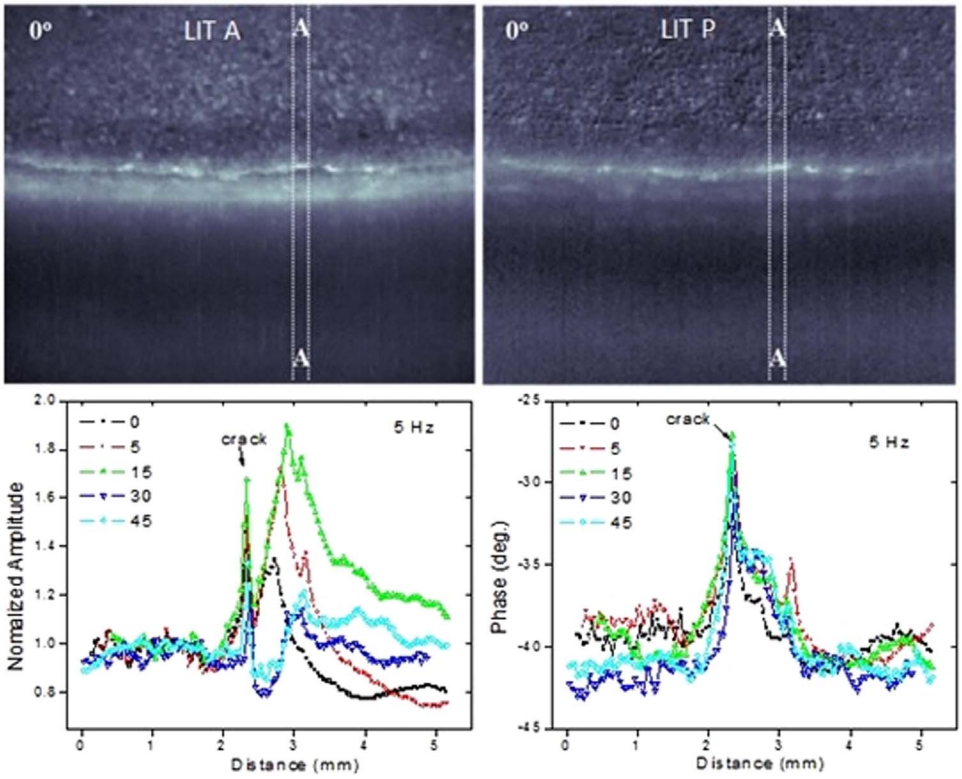

Fig. 4. Observation angle, α, effect on LIT (5 Hz) crack detection. Sample Sc1 LIT amplitude and phase (top) and section (A-A) profiles (bottom) at different observation angles.

averaged TWR/LIT pixel of two samples, with and without a crack. It was found that sample pitching, or observation, angle, α, Fig. 3(c), played an important role in image contrast enhancement and crack presence assessment. For example, in Fig. 4 the pixel profiles of LIT images yielded optimal crack detectivity at observation angle α=45°.

Modulation frequency bandwidth (range) affects crack detectivity. Using TWR pixel cross-section profiles, as shown in Fig. 5, the best crack contrast was obtained for 1 – 5 Hz chirp bandwidth which

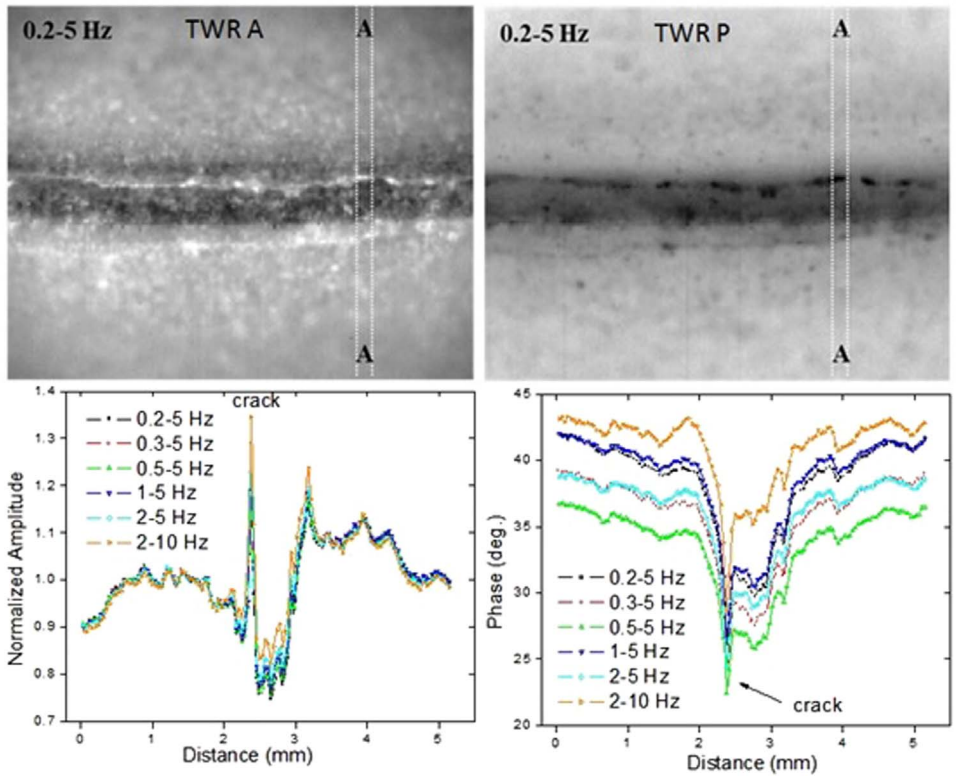

Fig. 5. Chirp frequency bandwidth effect on TWR crack detection. Sample Sc1 TWR amplitude and phase (top) and section (A-A) profiles at different chirp ranges.

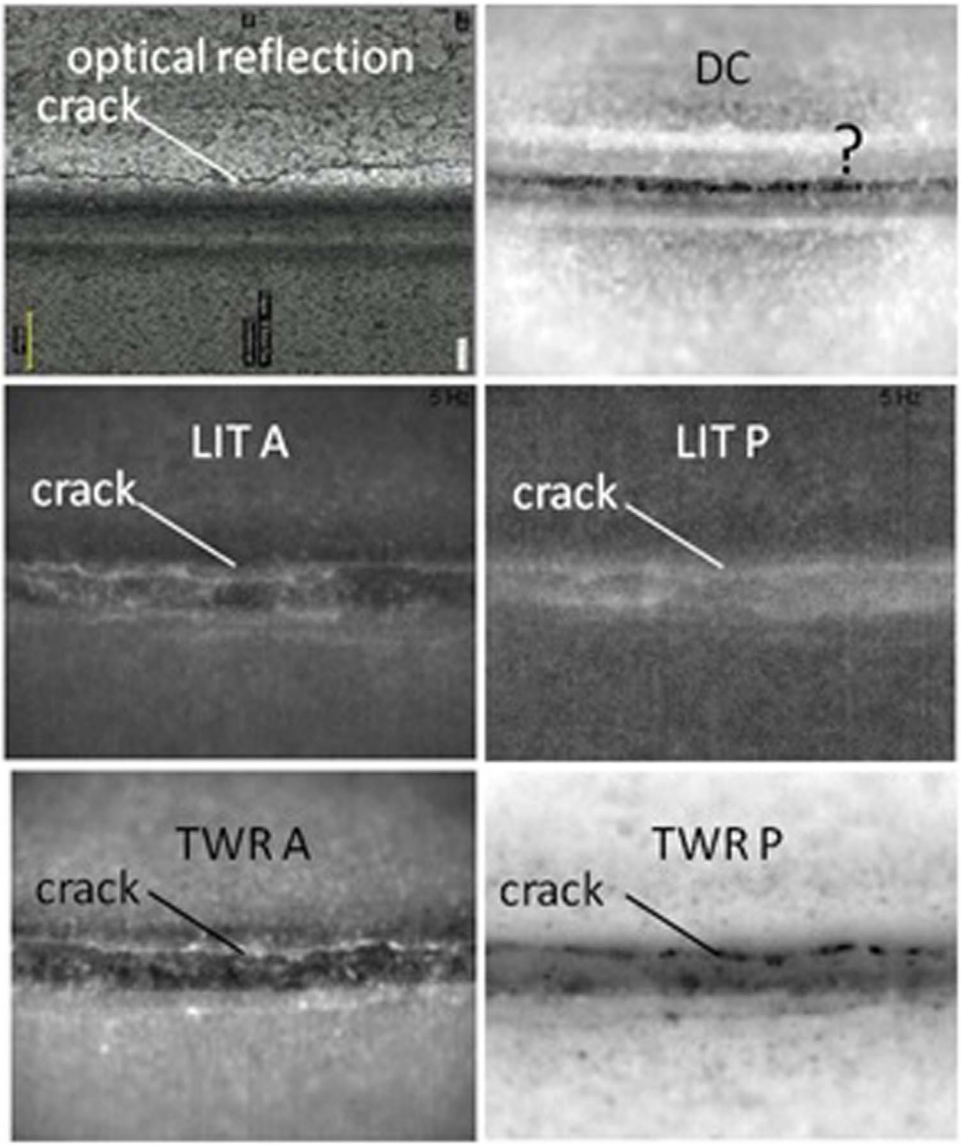

Fig. 6. Crack images using various imaging modalities.

generates ~ 0.5–1.1 mm penetration depth when 3.75 mm^2/s is used as the sprocket metal power diffusivity [30]. Using LIT pixel cross-section profiles, we also obtained 5 Hz as optimal modulation frequency.

4.2. TWRI/LITI open crack detection comparison

To compare the LIT and TWR imaging capabilities to detect cracks, green sample Sc1 with a crack was imaged with an optical microscope, DC thermography, LITI (5 Hz, α=45°) and TWRI (0.5–5 Hz, α=45°) amplitude and phase. Results are presented in Fig. 6. It can be seen that the DC thermal image cannot identify the crack. Both LIT and TWR amplitude and phase can detect the crack. The crack in amplitude images looks continuous like in the microscope image. Phase images (especially the TWR phase), however, show a discontinuous crack line. This is so because the phase image is a true thermal-wave image, more sensitive to the crack structure and boundaries below the surface and independent of surface optical features (reflectivity), while the amplitude image also contains surface optical contrast at the crack which tends to dominate the thermal-wave image and make it look like an optical reflection image. Compared with LIT, the TWR image exhibits better contrast in both amplitude and phase. The TWR phase better captures the crack geometry showing its inhomogeneous dimensions (narrow width) as clearly differentiated from other local features of the 90° corner. This is consistent with the depth resolved nature of the cross-correlation process. Fig. 7 shows how TWR amplitude images enhance the contrast and resolve surface defect features of green samples Sc1 and Snc1 compared to visible-range optical microscope images (as zoomed in on the right). Fig. 7(a) and (b) display various types of cracks in Sc1 while Fig. 7(c) and (d) are with and without Snc1 local defects, respectively. It can be seen from Fig. 7 that a crack is, in fact, an extended local defect. How to define cracks and local defects and differentiate between them are very important issues in industrial NDT applications and will be discussed in detail in Sect. 4.4.

As a major result of this research it was found that LIT and TWR are two imaging modalities with different merits and potential uses: LITI has higher signal to noise ratio, but images are slow to obtain, while TWRI has better depth resolution and image acquisition is significantly faster, more suitable for industrial inspection. In comparative inspection of images obtained with both modalities, such as in Figs. 4 and 5, it was concluded that spatial resolution and flaw imaging dynamic range are superior in the TWR cross-correlation phase image. For example, close inspection of the pixel profiles, Fig. 5, shows that the 0.5–5 Hz TWR phase image exhibits strong gradation details of the

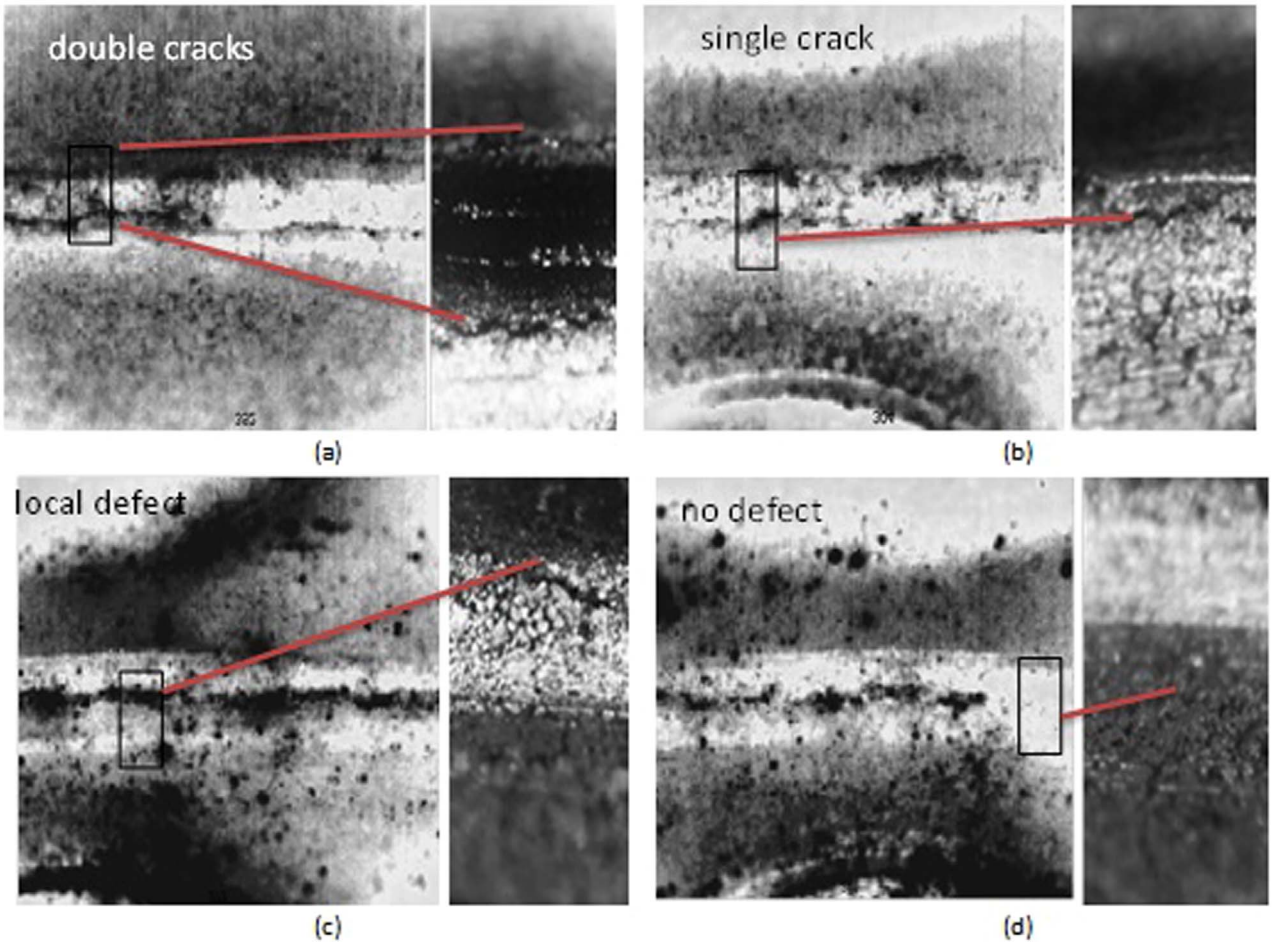

Fig. 7. Defect features of sample Sc1 ((a), (b)) and Snc1 ((c), (d)) obtained with TWRI (1–5 Hz, α=45°) amplitude and zoom-in optical microscope images. The narrow images were obtained with an optical microscope.

crack structure on the sides of the crack peak and a 15-degree dynamic range (between 22 and 37 degrees); the 5-Hz LIT phase image in Fig. 4 is very consistent with the TWR phase, however, the pixel profiles show much lower resolution of the gradations and a dynamic range of ~12 degrees (30 to ~ 42 degrees).

4.3. Crack detection validations

The foregoing TWR phase imaging results are typical of many TWR images and lead to the conclusion that the TWRI phase channel has optimal specificity, reliability and accuracy, adequately addressing the detection of surface-intersecting cracks in green (non-sintered) sprockets which would otherwise require lower contrast destructive optical microscopy of a sample region of interest (ROI) following sectioning. Fig. 8 shows TWR (1–4 Hz, α=45°) amplitude (TWR A) and phase (TWR P) images of samples Sc1 (with a crack) and Snc1 (without a crack) before and after sintering (upper half), and comparisons with cross-sectional optical reflection microscope images taken after sintering (lower half). For sample Sc1, Fig. 8(a), a crack exists before and after sintering (lower half). However, the phase image of the crack loses some contrast after sintering. This effect may be due to the fusion of narrow-width regions of the crack during the sintering process and/or due to the improved thermal diffusivity after sintering, which increases the thermal wavelength and reduces spatial and depth resolution. The microscope image does show the crack surface clearly and so does the TWRI amplitude, as expected, because a major contribution to amplitude contrast is due to the optical reflectivity of the surface. For sample Snc1, Fig. 8(b), some localized features appear (they may be contaminants or small localized cracks) before sintering, which disappear after high-temperature sintering, possibly due to the fusion of the small flaws. Theoretical studies of the thermal-wave field at the corner (unpublished) are consistent with a phase drop of 2–5 degrees across the corner in intact sprockets due to the increased thermal-wave conduction degrees of freedom (DOF) there. This change in thermal-wave DOF is best shown as a continuous line in the phase of the sintered sample, Fig. 8(b). This feature is very useful as a reference line for assessing the presence of a continuous irregular crack line appearing as a second line adjacent and parallel to the smooth reference line, as shown in the phase images of Fig. 8(a) and (b), with the latter image highlighting the presence of local flaws. The theoretical amplitude also exhibits a similar drop at the location of the corner. The result is the continuous smooth line which appears above the irregular crack line in Fig. 8(a), another reference feature for assessing the presence of continuous cracks. Here it is seen that another smooth line below the crack line is due to a corner feature on the counterbore vertical wall of the sprocket, visible in the optical microscope image. This feature may be an optical reflection of web surface features on the wall due to the increased reflectivity at the shallow grazing angle of the image. It is clearly seen as a second smooth line in the sintered Snc1 phase image of Fig. 8(b). From Fig. 8(a) it seems that the presence of an irregular long crack diminishes the contrast of this second smooth line feature. In summary, Fig. 8 demonstrates that TWRI can be used to detect cracks reliably in both green and sintered samples. The cracks can be recognized from TWR images as continuous zigzag lines, while local defects are displayed as random non-uniformities of the sample material.

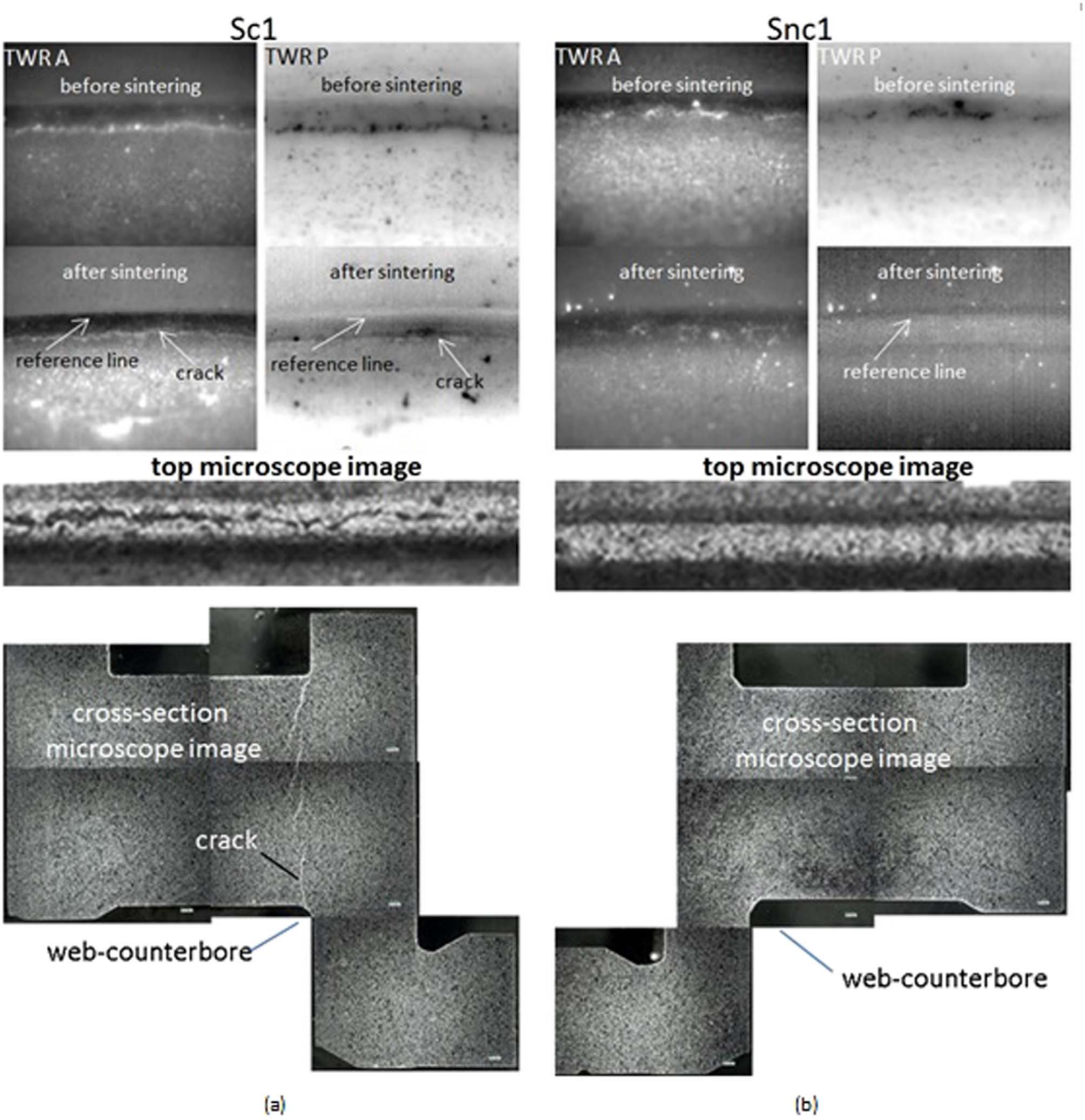

Fig. 8. Comparison between TWR (1–4 Hz, α=45°) images (A for amplitude and P for phase) of two samples Sc1 (a) and Snc1 (b) before and after sintering. The top and cross-section microscope images were taken after the samples were sintered.

To further prove the TWRI capability for green sample crack detection, another set of samples, Sc2 and Snc2, were imaged with TWRI around the whole web-counterbore circle (β=8° per frame, 45 frames in total for each sample). Then, the two samples were cross-sectioned at four sections each, in Sc2 (Sections 1–4) and in Snc2 (Section 5–8) as marked in Fig. 9. Optical microscope images of the cross sections were also taken. Comparisons between the TWR phase images and the microscope images of the cross sections are presented in Fig. 10. The top two rows (Fig. 10(a) and (b)), are TWR image frames of Sc2 and Snc2, respectively. The middle two rows (Fig. 10(c) and (d)) are the microscope images of the corresponding cross sections made along the dashed vertical lines. The squares indicate the ROI where the TWR images were taken. The bottom (Fig. 10(e) and (f)) are zoom-ins of the regions inside the squares. Both TWR and cross sectional images clearly show that only the Sc2 sample contains cracks, while they reveal local defects of various types both in Sc2 and Snc2. The local defects of Section 7 are so severe that they are comparable with cracks in Section 4. It was concluded that it may not be easy to separate cracks from local defects by simply viewing the TWR images. The original TWR images need additional processing to enhance the crack detection capability of this imaging modality. A method to do this is described below.

4.4. Automatic defect recognition

In order to differentiate cracks from local defects and intact samples, a statistical image analysis method for automatic defect recognition (ADR) was developed. In an ADR processed image, each ROI pixel is assigned to one of three states: potentially cracked, flawed (a local defect), or normal (intact), based on two selection criteria

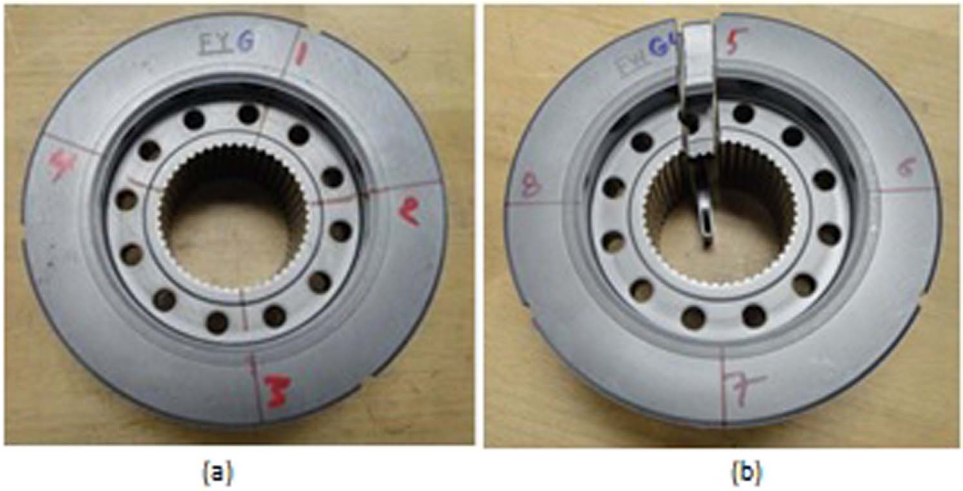

Fig. 9. Cross-section locations of (a) cracked (Sc2) and (b) crack-free (Snc2) green samples.

determined by user tolerance. Because any intermediate states between cracked, flawed and normal are erased, the contrast of ADR processed images is greatly enhanced. The statistical analysis output of each image frame is the average potential crack pixel percentage and the local defect pixel percentage and can be used for fast in-line inspection.

4.4.1. ADR algorithm

Algorithms for ADR and contrast optimization of flaws are a crucial part of any realistic industrial application of TWRI, as the flaw imaging goal is to assess the capability of dynamic thermographic imaging to *quickly and accurately* identify crack-seeding regions at high stress locations around the inner corners of PM components. In the automatic defect detection algorithm, a user first selects the starting and ending index of Y pixels to identify the ROI of the web-counterbore interface. In Fig. 11, 3 sets of phase raw data of Y pixels from 2 to 35 were selected out of 128 rows and the defects were expected around the middle of that ROI line. First, the software opens all frames (45) and calculates overall average and standard deviation (std-t) for phase (P_t) image data: $P_1 = P_t + X_2(P_{std-t})$, $P_2 = P_t - X_2(P_{std-t})$. Here P_t is overall phase average, $P_{std\text{-}t}$ is overall phase standard deviation, P_1 is upper limit and P_2 is lower limit for the phase range allowed in the ROI. X_2 is a constant that is used to optimize the presence of local defects. In Fig. 11, the selected X_2 was 0.5. Defects in the ROI phase data were detected by using the following test algorithm for each pixel, P_{ij}: If $P_2 \le P_{ij} \le P_1$ is true, then the datum P_{ij} is a normal point (intact) and it is replaced by the overall average phase (P_t). Otherwise, the datum P_{ij} is selected for the next test in the ROI. In the next test, each pixel P_{ij} in the ROI is checked again for the following condition: $P_2 > P_{ij}$. If true, the datum P_{ij} is selected for the final test; otherwise it is replaced with P_2.

In each ROI, phase data from line j were further analyzed to determine whether the pixel P_{ij} corresponds to a crack location, local defects or intact region. Fig. 11(a) shows one side (up to the turning point due to the presence of the 90-degree corner in the phase data) of 3 such lines from pixel line j. The slopes of these lines are used to identify whether that region is a crack, local defect or intact. The average slope of the solid-circle (green) curve is smaller than that of the open-circle (purple) curve because the overall extent of the change in the green trace is larger. Microscope images confirmed that the solid-circle curve phase data corresponded to an open crack, while the open-circle curve data didn't relate to any obvious cracks.

In the automated crack detection method, the solid-circle and solid square (red) curves in Fig. 11(a) were compared with the slope "$\hat{m}$" of the open-circle (intact reference) curve. The upper (m_{1in}) and lower (m_{2in}) limit of the reference slope "m_i" of the intact region was determined from the geometry of the sample interface; m_{1in}=30 and m_{2in}=40 were used in this comparison. If the slope was within the range $m2_{in} \le \hat{m} \le m1_{in}$, then the associated P_{ij} was identified as intact region and was replaced with a constant value (P_{in}=P_2). The upper (m_{1l}) and lower (m_{2l}) limits of the local defect slope were set based on the accepted range of local defects in the reference sample. If the local slope was outside the range of m_{1l} or m_{2l}, then $P_{ij} < 0.9P_2$ (cut-off marker of phase value for crack detection) were identified as cracks (green curve) and P_{ij} was replaced with a constant value (P_{crack}=$P_{2/4}$). Finally, if the slope was within the range $m2_l \le \hat{m} \le m1_l$, then that P_{ij} were identified as local defects and were replaced with a different constant value (P_{local} =$P_{2/2}$). The constant values for P_{crack} and P_{local} were selected for display purposes in the image to clearly distinguish those special data points P_{ij} from other features. The foregoing ADR test procedure was performed on both sides of the phase curve from line j (only the slope test from one side of line j is shown in Fig. 11). Fig. 11(b) shows the transformed (normalized) phase data after applying the automated crack detection technique. Fig. 12 shows a comparison between TWR (1–5 Hz, α=45°) original images and ADR processed ($m1_l$ =52, $m2_l$ =20) images of two green samples, Sc2((a) and Snc2(b), measured at β=88°. The regions with cracks, local defects and intact material are indicated with green, red and purple colors, respectively, in ADR processed images, in agreement with the color coding in Fig. 11(a). It can be seen that it is much easier to evaluate the quality of the two green samples with ADR processed images than the original TWR images: the Snc2 image is mainly composed of purple (intact) pixels with some red pixels (local defect), while the Sc2 image consists of extended regions of green (cracks), red (local defects) and purple (intact) pixels. The black zig-zag line indicates the intersection (corner) of the counterbore wall and the web, Fig. 2(b).

4.4.2. NDT with the ADR algorithm

TWR images (1–5 Hz, α=45°, 45 frames, 40-pixel ROI band) of two known samples Sc2 and Snc2 were first processed with the ADR algorithm using m_{1l} =52, m_{2l} =20. The output of the ADR analysis is presented in Fig. 13, where each data point represents the average from one frame. In Fig. 13(a), it is shown that the cracked sample Sc2 is well separated from the non-cracked sample Snc2 by potential crack pixel percentages, averaged at 9.7% for Sc2 and 0.25% for Snc2. The data points of the frames containing the cross sections (one section representing one line in a frame) in Fig. 10(e) are given as they track the flaw (crack) severity: Section 3 is the worst, followed by Section 2, Section 4 and Section 1. Fig. 13(b) displays local defect pixel percentages and their average values, 24.8% for Sc2 and 13.6% for Snc2. The data points of the frames containing Sections 5–7 in Fig. 10(f) also track flaw (local defect) severity: Section 7 is the worst

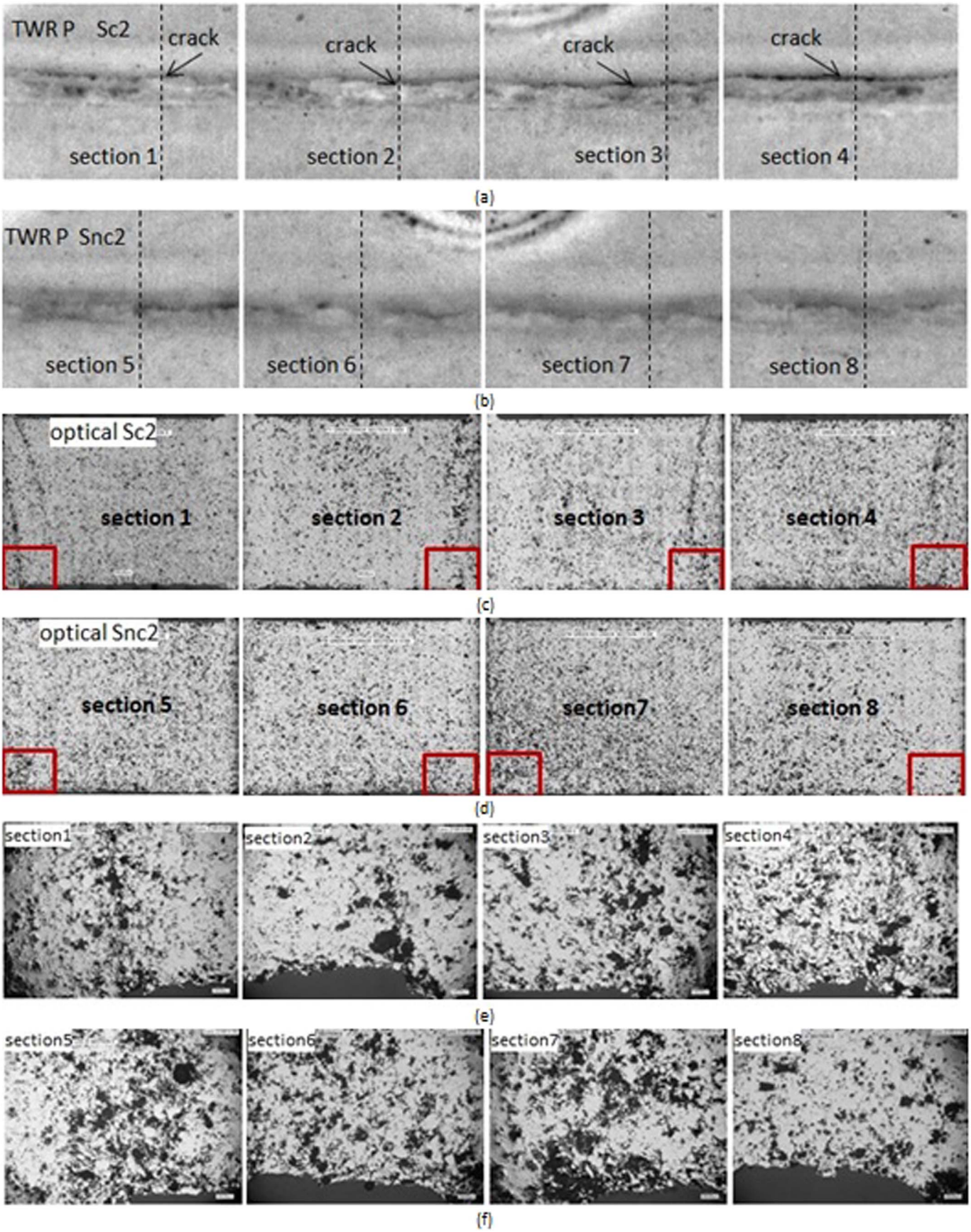

Fig. 10. Comparison between four TWR (10–15 Hz, α=45°) phase image frames of two samples Sc2 (a) and Snc2 (b) and corresponding microscope images of the cross sections, (c) and (d). The measured regions (square-marked) are zoomed in in (e) and (f). The dashed lines in (a) and (b) indicate where the samples were sectioned.

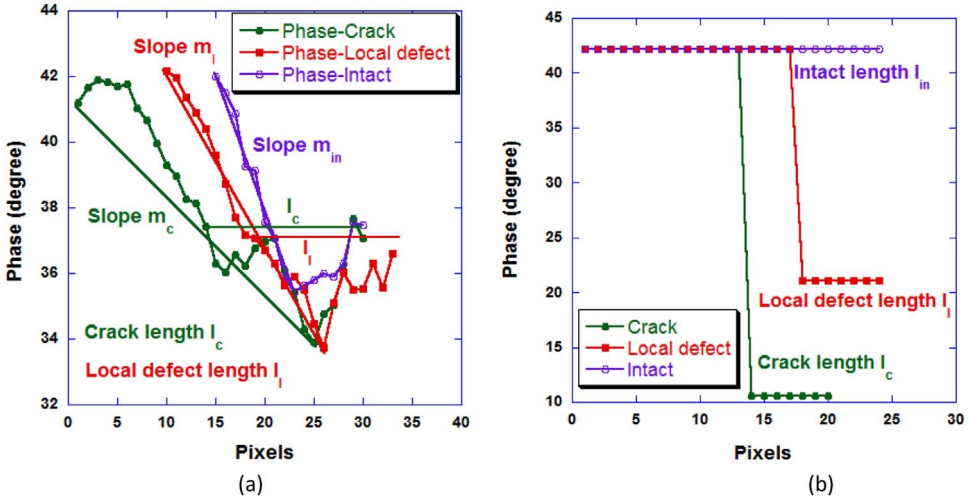

Fig. 11. Method of identifying cracks, local defects and intact regions in phase images. (a) crack (solid-circle), local defect (solid-square) and intact (open-circle) phase data. (b) Processed phase of cracked, locally defective and intact regions following automatic defect recognition (ADR) analysis. The ADR method is described in the text.

and followed by Section 5 and Section 6. The data point from section 8 has a higher value than expected when compared with its image in Fig. 10(f). This might be because the neighbouring lines in that frame show relatively high local defects. Fig. 13(a) indicates that the selection criteria m_{1l} =52, m_{2l} =20 are optimal because almost all the flaws in Snc2 are recognized as local defects (0.25% cracks and 13.6% local defects), in agreement with the manufacturer's identification. In this case, the threshold for labeling the sample as one with cracks should be taken as 0.25% potential crack pixel percentage (PCPP). Samples registering above 0.25% PCPP should be considered to have cracks.

To verify that the above statistical analysis is broadly valid, the TWR images of another set of intact (not sectioned) samples (two for each set), Sc3 and Snc3, were processed with the ADR algorithm under the aforementioned conditions. The PCPP and local defect results are presented in Fig. 14. The figure illustrates that the Sc3/Snc3 set can be separated by their average PCPP, 21.8% for Sc3 and 2.4% Snc3 (Fig. 14(a)) and their average local defect percentage (47.7% and 25.6%). Sc3 has higher percentage of PCPP and local defect percentage than Snc3. However, Snc3 is recognized as a sample with cracks because its PCPP is above the crack recognition threshold (0.25% PCPP), which contradicts the manufacturer's identification. This implies that if the threshold is kept at 0.15% PCPP, the current selection range (m_{1l}=52, m_{2l} =20) is too narrow because approx. 2.15% more local defects in Snc3 which are tolerable to the manufacturer, are placed inside the crack bearing category. In conclusion, the optimal selection criteria (m_{1l} and m_{2l}) should be determined by the user through statistical feedback from a large number of sample tests.

It was found that in order for the ADR image analysis program to run properly, the surface of green samples must be cleaned (e.g. using an air blower) before TWR measurements, to avoid erroneous outcomes. As an example, the above two sets of ADR processed samples Sc2/Snc2 and Sc3/Snc3 were cleaned before the TWR measurements using pressurized air followed by wiping with methanol-soaked tissue. Fig. 15 shows the same pixel profile of sample Sc3 before and after the cleaning. It can be seen that the profile before cleaning contains many spikes from contaminants, which, if not removed, will affect the ADR

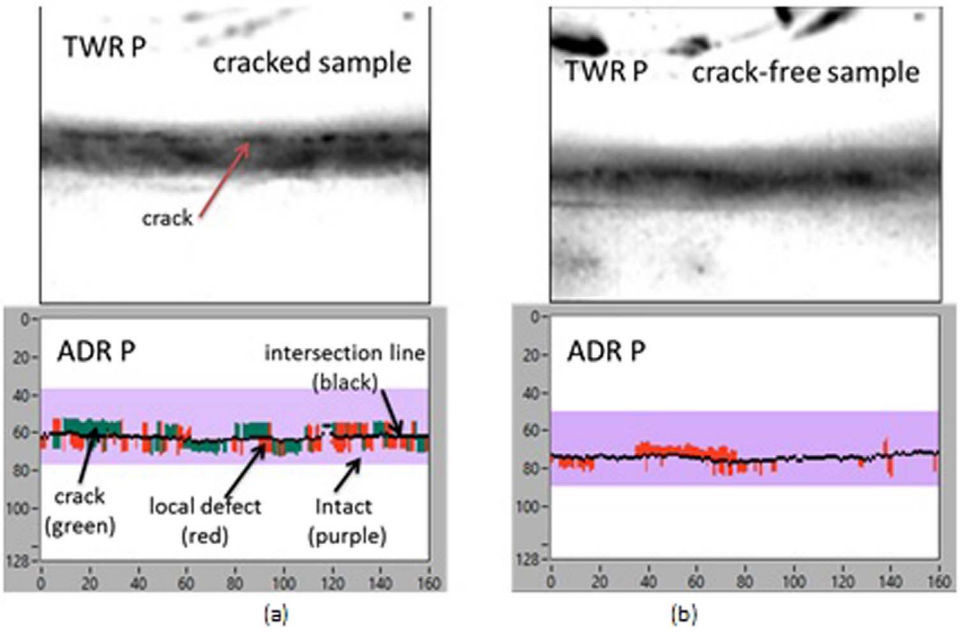

Fig. 12. Comparison between TWR (1–5 Hz, α=45°) original images (top) and ADR processed images (bottom) of two green samples: (a) Sc2; and (b) Snc2. The regions with cracks, local defects and intact material are indicated with green, red and purple color, respectively, in the ADR processed images.

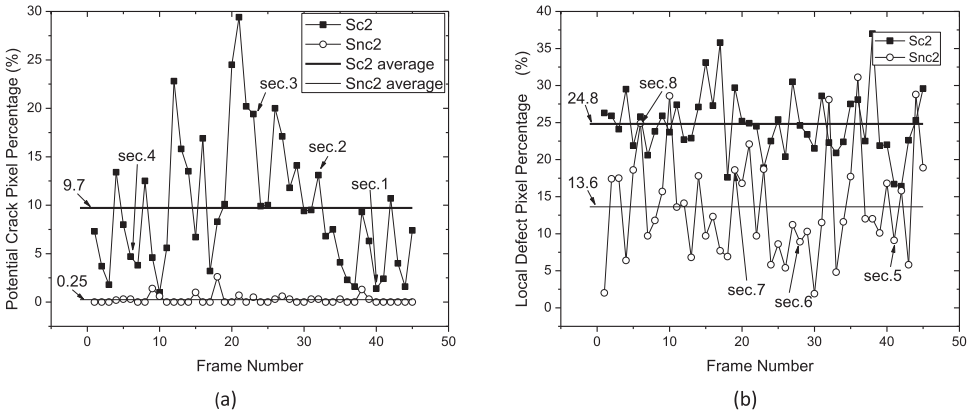

Fig. 13. Statistical TWR phase image analysis (m_{1l} =52, m_{2l} =20) to differentiate cracked (Sc2) and crack-free (Snc2) green samples. (a) Potential crack pixel percentage (PCPP) distribution of 45 images (covering 360 degrees in the web-counterbore circle); (b) local defect pixel percentage distribution of the same frames.

performance.

4.5. Optimized parameters for fast in-line inspection

Fast measurements and high image quality and reliability are essential for in-line flaw inspection. Thermalization time and number of sample images used for averaging are two factors that affect measurement speed. To optimize image quality, thermalization times of 60–90 s and a large number of averaged images (10–20) were used which resulted in relatively long measurement times (~2 min for TWR and ~3 min for LIT measurements at 5 Hz). To improve TWRI and LITI speed compatibility with industrial manufacturing rates, optimized thermalization time and number of averaged images were investigated using pixel cross-section profiles across a crack. It was demonstrated that for TWRI, the optimal thermalization time is 0 s and the image averaging number is 1 (no averaging). For LITI, a crack could also be detected without averaging with a 2-s thermalization time at 5 Hz. Thus, the LIT single frame imaging time could be reduced to 25 s at 5 Hz. With TWRI the single image/frame acquisition time could be reduced to ~5 s. The time for sampling the entire circumference at 8-degree (45) intervals was 4.75 min. This is still too long for real-time inspection. The closest inspection speed acceptable for in-line utilization of TWRI with the present system appears to be double the component production time (~20 s), using only four 90° intervals. Further decrease in image acquisition time is possible by use of a faster data processing computer and optimization of the LabVIEW ADR algorithm.

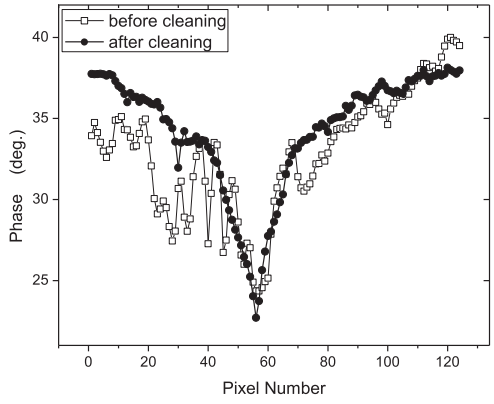

Fig. 15. Cleaning effect on sample Snc3 TWR phase pixel profile. The solid-circles and open-squares are TWR phase pixel profiles measured before and after the sample was cleaned.

5. Conclusions

Cracked and crack-free automotive industrial PM components (transmission sprockets) were inspected in their green state using thermal-wave-radar imaging (TWRI), and results were compared it with lock-in thermography imaging (LITI). High image contrast was achieved under optimized measurement conditions such as laser illumination position and uniformity, modulation frequency bandwidth, and sample orientation. The superiority of TWRI over LITI in flaw detection resolution and speed was demonstrated. TWRI is 1.5 times as fast as LITI and TWRI contains significantly more depth and

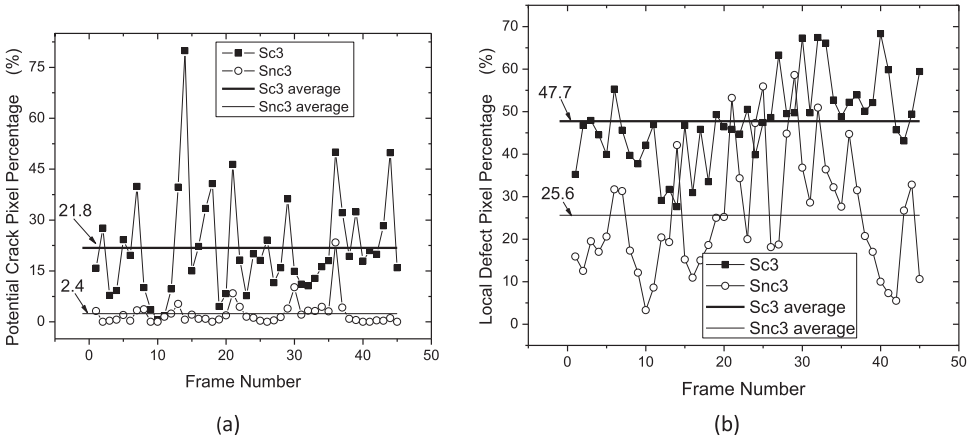

Fig. 14. Statistical analysis of ADR processed TWR phase image (PCPP, (m_{1l} =52, m_{2l} =20) of two cracked and crack-free green samples Sc3/Snc3: (a) PCPP; and (b) local defect pixel percentage.

spatially resolved information than LITI. The crack detection capability of the TWR phase image was validated by cross-sectional images of two sets of cracked/crack-free green samples which were sectioned in their green and sintered states after TWR measurements. To apply the TWRI technique to *reliable* industrial fast in-line inspection, an automatic defect recognition image processing (ADR) method was developed to differentiate cracks from local defects which may not develop into a crack at the sintering stage. The effectiveness of the ADR algorithm was verified by testing three sets of cracked/crack-free green sprockets. To the authors' best knowledge, this research establishes TWRI as the only green-sprocket manufacturing flaw imaging technology to-date capable of approaching the automotive industry's sprocket manufacturing speeds while delivering adequate spatial resolution and contrast for reliable flaw detection.

Acknowledgements

A. Mandelis gratefully acknowledges the NSERC Strategic Grants Program, an NSERC Discovery Grant and the Canada Research Chairs Program for financial support.

References

[1] Zenger DC, Cai H. Handbook of the common cracks in green P/M compacts, (Powder metallurgy research center. Worcester, MA: Worcester Polytechnic Institute; 1997.
[2] Bodnar JL, Menu C, Egée M. Detection of wear cracks by photothermal radiometry. Wear 1993;162–164:590.
[3] Bodnar JL, Egée M. Wear crack characterization by photothermal radiometry. Wear 1996;196:54.
[4] Burrows SE, Dixon S, Pickering SG, Li T, Almond DP. Thermographic detection of surface breaking defects using a scanning laser source. NDT E Int 2011;l44:589.
[5] Busse G, Wu D, Karpen W. Thermal wave imaging with phase sensitive modulated thermography. J Appl Phys 1992;71:3962.
[6] Wu D, Busse G. Lock-in thermography for nondestructive evaluation of materials. Rev Gen Therm 1998;37:693.
[7] Maldague XPV. Theory and practice of infrared technology for nondestructive testing. New York: Wiley-Interscience; 2001. p. 684.
[8] Breitenstein O, Warta W, Langenkamp M. Lock-in thermography: basics and use for evaluating electronic devices and materials. New York: Springer; 2003.
[9] Böhm S, Hellmanns M, Backes A, Dilger K. Lock-in thermography based NDT of parts for the automotive industry. J Adhes Interface 2006;7:10.
[10] Netzelmann U. Flying-spot lock-in thermography and its application to thickness measurement and crack detection; 2014.
[11] Busse G. Optoacoustic phase angle measurement for probing a metal. Appl Phys Lett 1979;35:759.
[12] Busse G. Techniques of infrared thermography: part 4. Lockin thermography. In: Maldague X, Moore PO, editors. 3rd edition. Nondestructive handbook, infrared and thermal testing, 3. Columbus, Ohio: ASNT Press; 2001. p. 718.
[13] Ibarra-Castanedo C, Maldague X. Pulsed phase thermography reviewed. QIRT J 2004;1:47.
[14] Ibarra-Castanedo C, Bendada AH, Maldague X. Thermographic image processing for NDT, In: Proceedings of the IV Pan American NDT Conference, (de END Buenos Aires, Argentina InAsociación Argentin); 2007.
[15] Benzerrouk S, Ludwig R. Infrared detection of defects in powder-metallic compacts. J Nondestruct Eval 2007;26:1.
[16] Benzerrouk S, Ludwig R. An infrared imaging approach for quality assurance in the powder metallurgy process, In: Proceedings of the world congress powder metallurgy & particulate materials, session NDE proceedings and methods, Washington, DC, 031363; June 2008. p. 8–12.
[17] Benzerrouk S. Active and passive thermography for the detection of defects in green-state powder metallic compacts [Ph.D. thesis]. Worcester Polytechnic Institute; 2011.
[18] Tolev J, Mandelis A. Laser photothermal non-destructive inspection method for hairline crack detection in unsintered automotive parts: a statistical approach. NDTE Int 2010;43:283.
[19] Munidasa M, Mandelis A. Photothermal imaging and microscopy. In: Mandelis A, editor. Progress in photothermal and photoacoustic science and technology. New York: Elsevier; 1992, [chapter 6].
[20] Mandelis A. Diffusion-wave fields: mathematical methods and green functions. New York: Springer-Verlag; 2001, [chapter 3].
[21] Tabatabaei N, Mandelis A. Thermal-wave radar: a novel subsurface imaging modality with extended depth-resolution dynamic range. Rev Sci Instrum 2009;80:034902.
[22] Farnett EC, Stevens GH. Pulse compression radar. In: Skolnik MI, editor. Radar handbook,. New York: McGraw-Hill; 1990, [chapter 10].
[23] Mandelis A. Frequency modulated (FM) time delay photoacoustic and photothermal wave spectroscopies. Technique, instrumentation, and detection. Part I: theoretical. Rev Sci Instrum 1986;57:617.
[24] Mandelis A, Borm MC, Tiessinga J. Frequency modulated (FM) time delay photoacoustic and photothermal wave spectroscopies. Technique, instrumentation, and detection. Part II: mirage effect spectrometer design and performance. Rev Sci Instrum 1986;57:622.
[25] Mandelis A, Borm MC, Tiessinga J. Frequency modulated (FM) time delay photoacoustic and photothermal wave spectroscopies. Technique, instrumentation, and detection. Part III: mirage effect spectrometer, dynamic range, and comparison to pseudo-random-binary sequence (PRBS) method. Rev Sci Instrum 1986;57:630.
[26] Mulaveesala R, Vaddi JS, Singh P. Pulse compression approach to infrared non-destructive characterization. Rev Sci Instrum 2008;79:094901.
[27] Tabatabaei N, Mandelis A, Amaechi B. Thermophotonic radar imaging; An emissivity-normalized modality with advantages over phase lock-in thermography. Appl Phys Lett 2011;98:163706.
[28] Velasquez-Hernandez R, Melnikov A, Mandelis A, Sivagurunathan K, Rodriquez-Garcia ME, Garcia J. Non-destructive measurements of large case depths in hardened steels using the thermal-wave radar. NDTE Int 2012;45:16–21.
[29] Tabatabaei N, Mandelis A. Thermal coherence tomography using match filter binary phase coded diffusion waves. Phys Rev Lett 2011;107:165901.
[30] Rombouts M, Froyen L, Gusarov A, Bentefour E, Glorieux C. Photopyroelectric measurement of thermal conductivity of metallic powders. J Appl Phys 2005;97:024905.